

# Split ring resonator resonance assisted terahertz antennas

Hossam Galal<sup>1, 2\*</sup>, Leonardo Viti<sup>2</sup>, and Miriam S. Vitiello<sup>2</sup>

<sup>1</sup> Department of Physics, Ain Shams University, Cairo 11566, Egypt

<sup>2</sup> NEST, Istituto Nanoscienze – CNR and Scuola Normale Superiore, Piazza San Silvestro 12, Pisa, I-56127

\* [hgalal@sci.asu.edu.eg](mailto:hgalal@sci.asu.edu.eg)

**Abstract:** We report on the computational development of novel architectures of low-impedance broadband antennas, for efficient detection of Terahertz (THz) frequency beams. The conceived Split Ring Resonator-Resonance Assisted (SRR-RA) antennas are based on both a capacitive and inductive scheme, exploiting a 200  $\Omega$  and 400  $\Omega$  impedance, respectively. Moreover, the impedance is tunable by varying the coupling parameters in the exploited geometry, allowing for better matching with the detector circuit for maximum power extraction. Our simulation results have been obtained by assuming a 1.5 THz operation frequency.

---

## References and links

1. R. Köhler *et al.* “Terahertz semiconductor heterostructure laser,” *Nature* **417**(156), 156-159 (2002).
  2. H.C. Liu *et al.* “Terahertz quantum-well photodetector,” *Appl. Phys. Lett.* **84**, 4068-4070 (2004).
  3. Gabor, N. M. *et al.* “Hot carrier-assisted intrinsic photoresponse in graphene,” *Science* **334** (6056), 648-52 (2011).
  4. F. Sizov *et al.* “THz radiation sensors,” *Opto-Electronics Review* **18** (1), 10-36 (2010).
  5. A. Rose, in *Concepts in Photoconductivity and Allied Problems*, Krieger (1978).
  6. M. Dyakonov, M. Shur, Detection, “Mixing, and Frequency Multiplication of Terahertz Radiation by Two-Dimensional Electronic Fluid,” *IEEE Trans. Electron. Devices* **43** (3), 380-387 (1996).
  7. Richter, H. *et al.* “Integrated planar log-spiral antenna at terahertz waves,” presented at IEEE International Workshop on Small Antennas and Novel Metamaterials, (March 2005).
  8. M. Vitiello *et al.* “Graphene field-effect transistors as room-temperature terahertz detectors,” *Nature Mater.* **11**, 865-871 (2012).
  9. Lee, Yun-Shik, “Continuous-Wave Terahertz Sources and Detectors,” in *Principles of Terahertz Science and Technology*. Springer US (2009).
  10. Leonardo Viti *et al.* “Nanowire Terahertz detectors with a resonant four-leaf-clover-shaped antenna,” *Optics Express* **22**(8), 8996-9003 (2014).
  11. Hailu, D.M. *et al.* “Simulation of bow-tie THz antenna using hybrid finite element method and spectral ray tracing technique,” presented at *IEEE International Conference on Infrared, Millimeter, and Terahertz Waves* (Sept. 2009).
  12. Chao Zhang, “Optical simulation of terahertz antenna using finite difference time domain method,” M.S. thesis, Rochester Institute of Technology (2014).
  13. Gay-Balmaz, Philippe; Martin, Olivier J. F. “Electromagnetic resonances in individual and coupled split-ring resonators,” *Journal of Applied Physics* **92** (5), 2929–2936 (2002).
-

## 1. Introduction

Terahertz (THz) frequency waves (0.1-10 THz, 30-3000  $\mu\text{m}$ ) are capable of penetrating numerous commonly used dielectric materials, otherwise opaque for visible and mid-infrared light, opening the path to a variety of strategic applications in biology, chemistry, medicine, astronomy and security. The full technological development of commercial THz systems requires the implementation of efficient and reliable sources and detectors. Quantum Cascade Laser (QCL) research is very active, and efficient sources have been realized in the range (1.5-4 THz) [1]. However, the realization of efficient THz detectors at room temperature (RT) is currently underway and remains a major challenge for the exploitation of the benefits of this frequency range.

The key principle on which photodetection relies is the conversion of absorbed photons into a measurable electrical signal. This has been realized in Field Effect Transistor (FET) devices through several mechanisms: the photovoltaic effect [2], the photo-thermoelectric effect [3], the bolometric effect [4], the photogating effect [5] and the plasma-wave-assisted mechanism [6]. Among these, and with the rise of novel two-dimensional electron gas materials, detection of THz radiation in FET devices based on the plasma-wave-assisted mechanism is an emerging topic. According to the model proposed in 1996 by Dyakonov and Shur [6], a finite *dc* voltage is generated in a FET in response to an oscillating electric field coupled between source (S) and gate (G) electrodes. The FET channel, hosting a 2D electron gas, acts as a cavity for plasma waves (collective density oscillations), and rectification arises from the nonlinear response of the 2D electron gas. Two operational regimes, resonant and broadband, can be defined according to the geometrical dimensions of the FET channel and the 2D electron gas properties. Beside this, the sub-wavelength size of the FET channel at THz frequencies requires a proper coupling element to funnel the incident THz radiation onto the FET. This can be easily realized by employing metallic resonators that, once contacted to the S and G electrodes, can act as receiving antenna for a THz beam. Accordingly, the figures of merit of a FET detector, operated in plasma-wave mechanism, are strongly dependent on the antenna efficiency and geometry.

Conventional microwave antenna geometries have to be downscaled to operate at THz frequencies. Commonly used schemes are: spiral [7], log-periodic [8], dipole [9], four-leaf [10], and bow-tie [11] antennas. The linear downscaling of most architectures is however not efficient at THz frequencies, leading to a major performance deterioration, caused by the increased kinetic energy of the conduction electrons. Novel antenna designs are therefore needed to fully exploit the benefits of the THz-frequency range. The antenna response can be tailored by controlling the paths of its surface currents. A common practice to realize this is to selectively remove areas of the antenna surface metal [12]. An alternative novel approach is by using auxiliary circuits to remotely manipulate the antenna surface currents. This can be accomplished with the aid of Split Ring Resonators (SRRs) [13] via electric circuit coupling. We here introduce a new generation of tunable-low-impedance Split Ring Resonator-Resonance Assisted (SRR-RA) antennas for efficient RT detection in FETs operating at 1.5 THz. Among the aforementioned antenna topologies, the bowtie antenna is renowned for its low impedance and self-complementary structure support, and can be linearly downscaled from the microwave region to operate in the THz region. However, its geometry has to be conveniently modified to be compatible with SRR integration to allow for performance improvements.

## 2. Contour-like bowtie antenna

Circuit coupling is conventionally optimum along straight parallel lines, demanding contour-like bow-tie arms rather than solid filling. Fig. 1 shows a contour-like bow-tie antenna design simulated with a Microwave Studio (CST) software; the antenna consists of two contour squares

with their diagonals vertically aligned a distance  $L$  apart from each other. The reason for choosing a square geometry is for its  $90^\circ$  corners, allowing for a self-complementary structure while preventing the design simplicity. The contour width  $W_c$  is a parameter that defines the main resonant mode of the antenna, together with the diagonal length  $D$  of the square. Table I lists the antenna relevant geometrical parameters, optimized for operation at a fixed frequency of 1.5 THz.

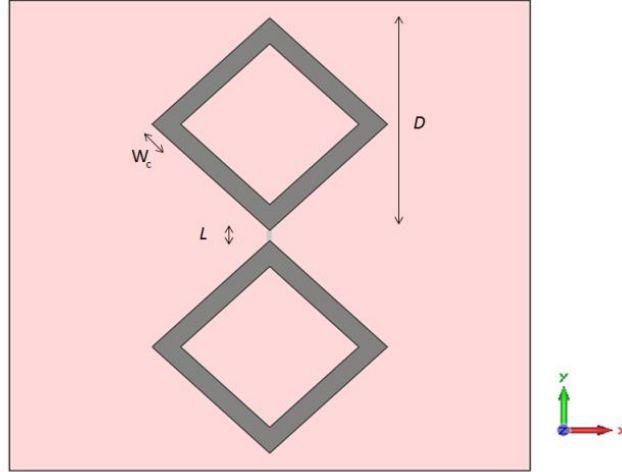


Fig. 1. Top view of the contour-like bow-tie antenna with its relevant geometrical parameter indicated.

Table 1. Antenna and substrate relevant parameter values

Symbol	Quantity	$\mu\text{m}$
$D$	contour diameter length	29.2
$L$	gap between arms	2
$W_c$	contour width	5
$t_{Au}$	antenna gold thickness	0.1
$t_{SiO2}$	oxide epilayer thickness	0.3
$t_{Si}$	substrate thickness	300

In order to estimate the antenna impedance we simulated the antenna return loss (Sff) as a function of frequency, when the THz excitation is generated by a feeder connected between the two antenna arms. By sweeping the feeder resistance  $R_f$  we found that the antenna impedance is approximately comparable to that of a conventional bowtie, having maximum power coupled to the antenna at  $R_f$  equal to  $50 \Omega$  (Fig. 2).

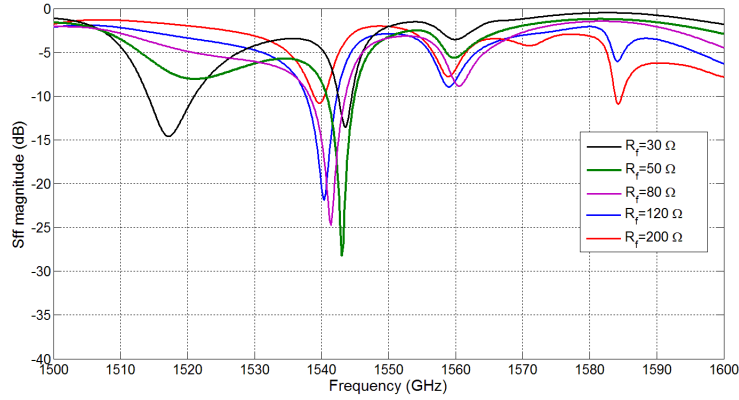


Fig. 2. Contour antenna return loss Sff, for different feeder impedance  $R_f$ .

In order to suppress the waveguide modes, the contour antenna has also been investigated in reception mode, by simulating transmission (S21) due to a plane wave ( $\mathbf{E}_y$ ) excitation in a metamaterial periodic array. Transmission simulations have been performed in the two configurations detailed below.

### 2.1 Open-circuit feeder port

In a first simulation run, the two arms of the antenna are electrically disconnected. The antenna resonant modes can be clearly observed from this simulation, through the well defined absorption peaks and the corresponding electric field distribution at the feeding neck. Fig. 3 shows an overlay between the antenna return loss Sff (50  $\Omega$  feeder) and transmission response S21, with an open circuit feeder port.

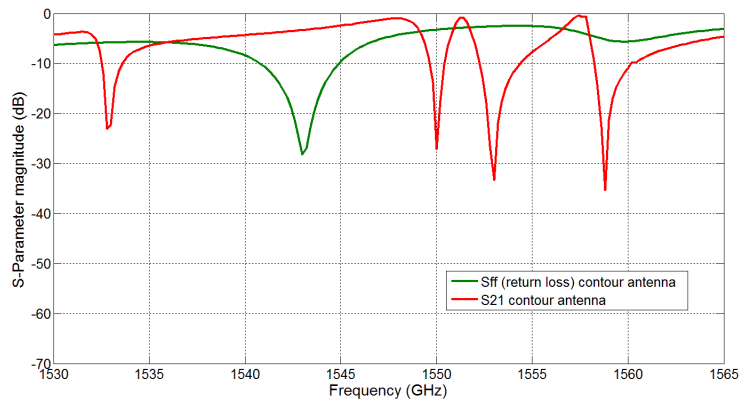


Fig. 3. Comparison between the contour antenna's return loss Sff and transmission response S21.

Additional higher order modes appear in close proximity of the red shifted main mode (1532 GHz), with respect to the return loss response. The frequency scale has been limited to the 1530-1565 GHz range to allow for very fine solver meshing, in order to better resolve the wavelength. The  $\sim 0.06\%$  frequency shift and the difference in number of modes between the antenna return loss and the transmission measurement are attributed to the background condition difference between the transmission and reception modes.

## 2.2 Matched impedance feeder port

This second simulation configuration provides a reliable way to verify whether the antenna absorption peaks shown in Fig. 3 are resonant modes or metamaterial losses. A  $50\ \Omega$  matched port (port 3) connected in place of the feeder gives rise to high S31 (fraction of incident radiation transmitted through port 3) amplitudes when the electromagnetic power is efficiently collected by the contour antenna, i.e. in correspondence with the antenna resonance modes, as illustrated in Fig. 4. We here adopt the linear scale plot to better unveil the shape of the peaks.

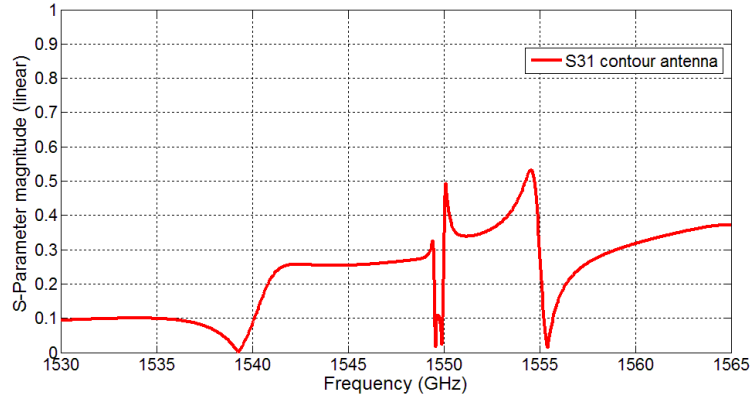


Fig. 4. S31 response for contour antenna, exposed to a plane wave ( $E_y$ ).

Indeed, four spectral windows with enhanced transmission can be observed in correspondence with the open circuit feeder response. The transmission windows exhibit a plateau with a 2 to 5 orders of magnitude broader bandwidth, than the absorption peaks; apart from the second order mode centralized around 1552 GHz, featuring two edge shoots and having nearly a same linewidth of 5 GHz. Maximum energy is extracted by the antenna between 1550 GHz and 1555 GHz (note that only 1% of the power is extracted for the main mode). For a  $1W/[(130\ \mu m \times 130\ \mu m)$  unit cell surface area] incident wave, a maximum of 27.04% of the incident power can be collected by the antenna, in case of perfect matching.

Before moving on to the incorporation of SRR, observing the antenna current distribution would serve as a good reference for understanding the impact of the SRRs on the overall design. Fig. 5 depicts the surface current distribution for the main mode at two phases ( $90^\circ$  and  $270^\circ$ ) when the open circuit feeder port configuration is employed. For the two half cycles, the currents along the Y-axis of the antenna are unidirectional in both arms and their branches merge

together at the contour corners along the Y-axis. The current distribution of the other peaks has the same trend.

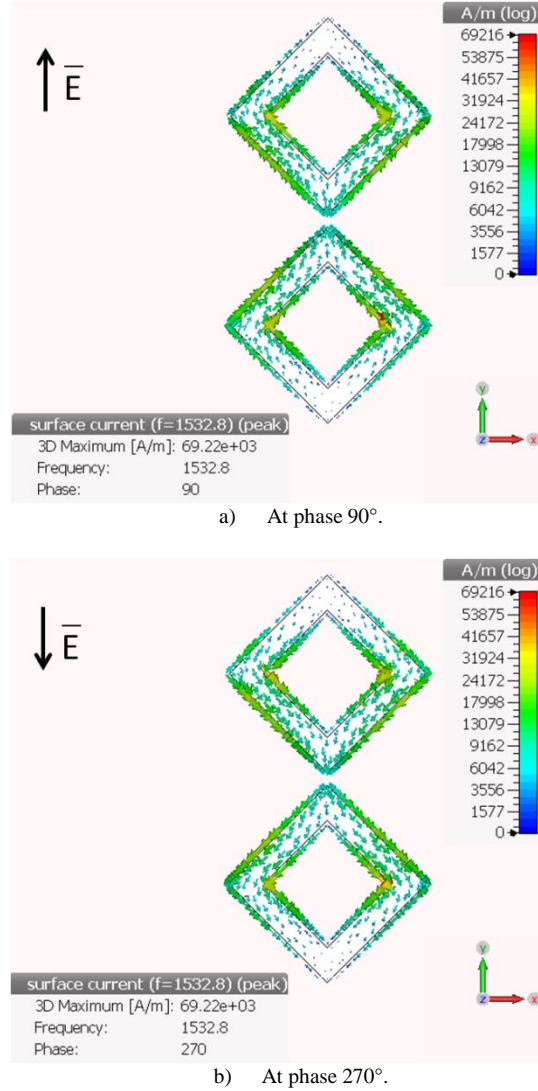
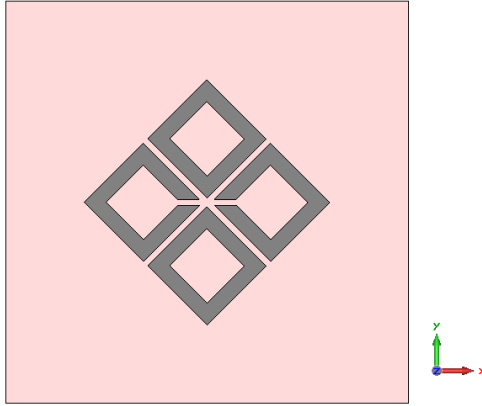


Fig. 5. Currents generated in a contour antenna upon exposure to a plane wave ( $\mathbf{E}_y$ ), for the main mode.

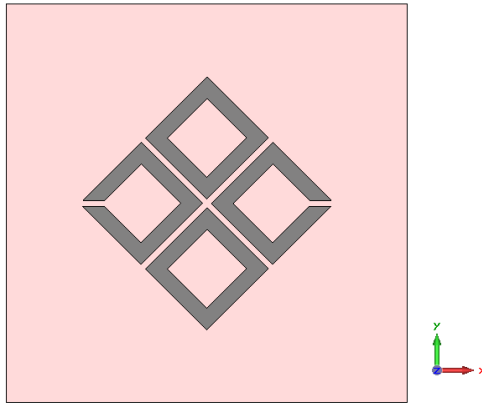
With the addition of two side SRRs, as depicted in Fig. 6, two SRR-RA configurations can be defined: a capacitive and an inductive one. Depending on their position, the SRR cuts determine the current direction in the SRR and the subsequent electric and magnetic field orientation. The SRRs have the same dimensions as the contour, placed a *coupling width* of  $2 \mu\text{m}$  apart from the contour, with a  $2 \mu\text{m}$  *cut*.

To better understand the impact of the SRRs on the contour, we consider the antenna operating in reception mode. For an incident plane wave ( $\mathbf{E}_y$ ) and during its positive half cycle, the currents in the SRRs can either be clockwise or counter-clockwise depending on whether the

cuts are on the left hand side or the right hand side of the SRR, respectively. Fig. 6a corresponds to the case where a clockwise current is excited in the left SRR, while a counter-clockwise current is excited in the right SRR. In Fig. 6b, the individual SRR currents are reversed with respect to the latter case. In principle, the two configurations support simultaneous capacitive and inductive coupling, but one is dominant at the expense of the other, since they give rise to opposite and competing contributions.



a) Capacitive SRR-RA: clockwise current in left SRR, and counter-clockwise current in the right SRR.



b) Inductive SRR-RA: counter-clockwise current in left SRR, and clockwise current in the right SRR.

Fig. 6. Two SRR-RA configurations corresponding to the different SRRs' cut position.

The SRRs geometry, together with the *coupling width*, define the strength and the shares of each coupling mechanism. In particular, coupling is sensitive to the *coupling width* and the relative ratio  $W_c/W_{SRR}$ , where  $W_c$  is the width of the contour and  $W_{SRR}$  is the corresponding width of the SRR. In our case  $W_c/W_{SRR} = 1$ .

With the current distribution of the stand-alone contour antenna in mind, each SRR-RA configuration is here separately investigated.

### 3. Capacitive split ring resonator resonance assisted antenna

In the experimental configuration depicted in Fig. 6a, capacitive coupling is dominant, since coupling is optimum along parallel conductors with opposite currents. This condition is fulfilled when the SRRs cuts are external, as shown in Fig. 7.

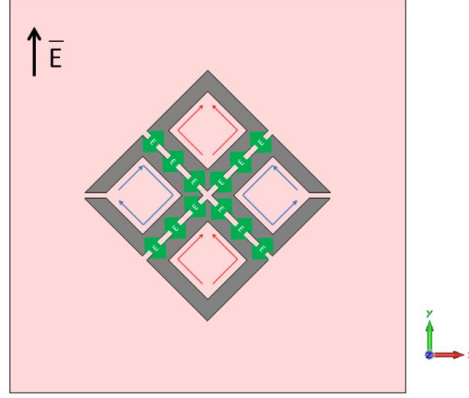


Fig. 7. Circuit analysis for the capacitive SRR-RA configuration, for a positive half cycle. SRR current (blue) contour current (red). Capacitive coupling gives rise to the electric field distributions (green) along the counter-SRR sides.

The SRRs and the contour are simultaneously excited by the incident plane wave ( $E_y$ ), and give rise to the currents indicated by the blue and red arrows, respectively, for a positive half cycle. The currents in each element are reinforced by the mutual capacitive coupling along the SRR-contour sides. A high intensity electric field distribution develops along the parallel coupling sides, indicated by the green arrows. Both the SRRs and the contour are independently excited by the incident wave, but their currents harmonically oscillate together, driven by the coupling electric field, resulting in an overall collective behavior. For the negative half cycle, the mechanism is the same, but in reverse direction.

As in the case of the contour antenna, we performed transmission simulations for the capacitive SRR-RA configuration using an open-circuit and matched impedance feeder port. The return loss simulation analogous to that reported in Fig. 2 for the contour antenna is not meaningful in this case, since it does not give information about the contributions of the SRRs. In fact, exciting the contour elements by a feeder port, will induce currents in the SRRs whose orientation is solely defined by the excitation direction, regardless of the SRRs cut position.

#### 3.1 Open-circuit feeder port

The integrated antenna absorption modes can be observed in Fig. 8 and compared to the corresponding modes for the stand-alone contour (Fig. 3). All modes show at least a -10 dB amplitude enhancement, accompanied by a slight blue shift, 8 GHz and 1 GHz, for the main and second order modes, respectively. Two intermediate modes develop at 1553 GHz and 1557 GHz.

The working principle of the SRRs can be extrapolated from the field images. Fig. 9 illustrates the electric field intensity distribution for the main mode for a full excitation cycle. The SRRs and the contour are simultaneously resonant, as can be seen by the very high electric field

intensity in the cut and the contour gap regions. The electric field intensity along the trenches between the SRRs and the contour refers to the capacitive coupling between the SRRs and the contour itself.

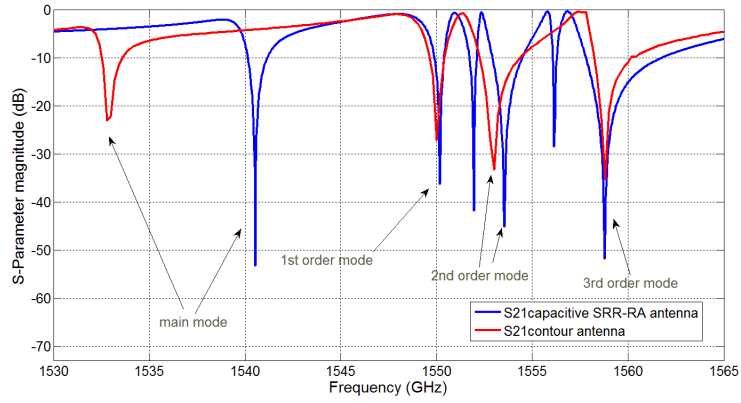
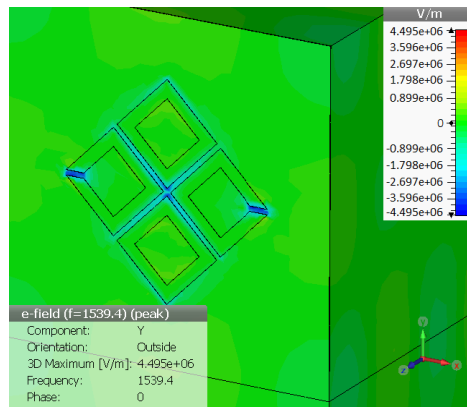
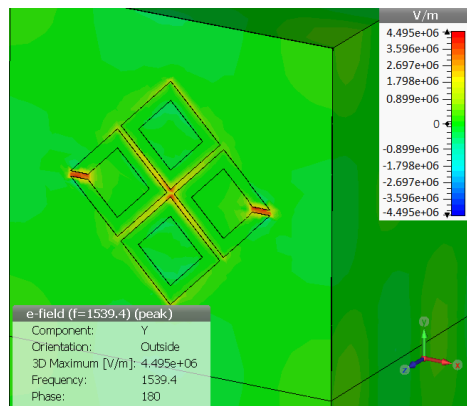


Fig. 8. Overlay of the S21 responses for the contour and the capacitive SRR-RA antennas.



a) At phase  $0^\circ$ .



a) At phase  $180^\circ$ .

Fig. 9. Electric field intensity distribution for the main mode for a full excitation cycle.

### 3.2 Matched impedance feeder port

The overall impedance of the integrated antenna was found to have increased to  $\sim 200 \Omega$ , upon incorporation of the SRRs. The resonance peaks observed earlier in Fig. 8 can be verified in a similar manner for the contour antenna, by measuring the transmission through a  $200 \Omega$  matched feeder port (port 3), as shown in Fig. 10. Six well defined S31 peaks can be observed, in this latter case, in correspondence with the six S21 peaks revealed in Fig. 8. In contrast with the contour antenna, the performance improvements operated by the SRR is clearly unveiled by the peaks amplitude enhancement, where the main, first and last order contour antenna modes are almost doubled. Furthermore, the additional peaks observed provide an increased operational bandwidth.

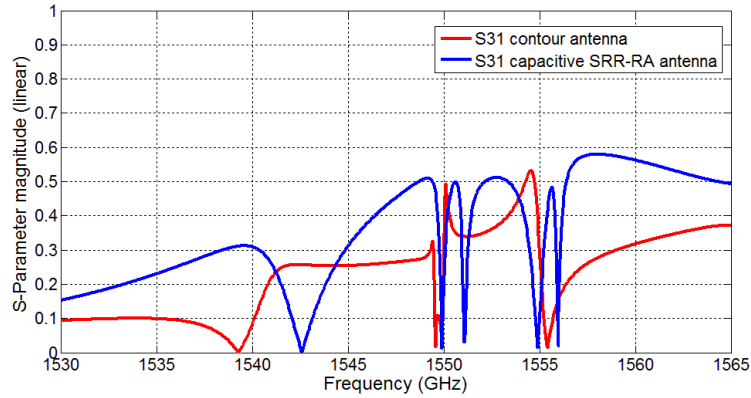


Fig. 10. Overlay of the S31 responses of the contour and the capacitive SRR-RA antennas.

## 4. Inductive split ring resonator resonance assisted antenna

By swapping the position of the SRR cut from the outside to the inside, the SRR currents along the coupling sides are aligned in the same direction as the contour currents, giving rise to dominant inductive coupling (Fig. 11).

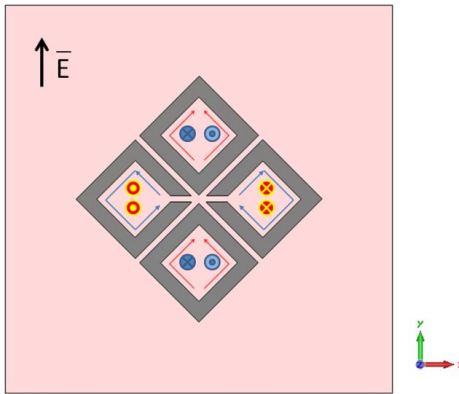


Fig. 11. Circuit analysis for the inductive SRR-RA configuration, for a positive half cycle. SRR current (blue) and contour current (red). SRRs' current inductively couple to the contour through (blue) magnetic field distributions, while the contour currents couple back to the SRR through the (red) magnetic field distributions.

The SRRs and the contour are simultaneously excited by the incident plane wave ( $E_y$ ). The resultant currents are indicated by blue and red arrows, respectively, for a positive half cycle. By applying the right hand rule to the individual currents, and knowing that a magnetic flux entering the plane of a closed loop generates clockwise currents while counter-clockwise currents are generated when the flux is exiting, the consequent magnetic fields are aligned together in a constructive manner, reinforcing each other's current. For the negative half cycle, the mechanism is the same, but in reverse direction.

#### 4.1 Open-circuit feeder port

The antenna absorption modes are shown in Fig. 12, and compared with the corresponding ones in the contour geometry.

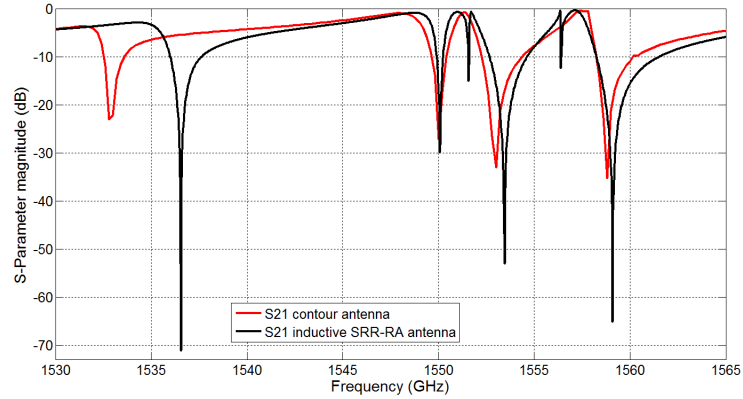


Fig. 12. Overlay of the S21 responses for the contour and the inductive SRR-RA antennas.

As clearly shown in the graph, the main result is an amplitude enhancement accompanied by a slight blue shift. The two intermediate peaks observed in the capacitive SRR-RA configuration (Fig. 8), are here still present but with a reduced amplitude. The working principle of the SRRs can be understood by considering the field images of the main mode, shown in Fig. 13. The resonance strength of the SRRs, observed from the electric field intensity in the cut region, is moderate compared to that in the gap between the two contour arms. This reduced SRR oscillatory strength can be explained by means of the inductive coupling efficiency between the SRRs and the contours. The inductive coupling strength from the SRRs to the contours is strong, while the inductive back coupling from the contours to the SRRs is weak, resulting in an unbalanced energy exchange between the SRRs and the contours. This claim has been confirmed by the magnetic field intensity distribution, as shown in Fig. 14, where a higher intensity can be observed in the contours compared with the SRRs.



a) At phase 0°.

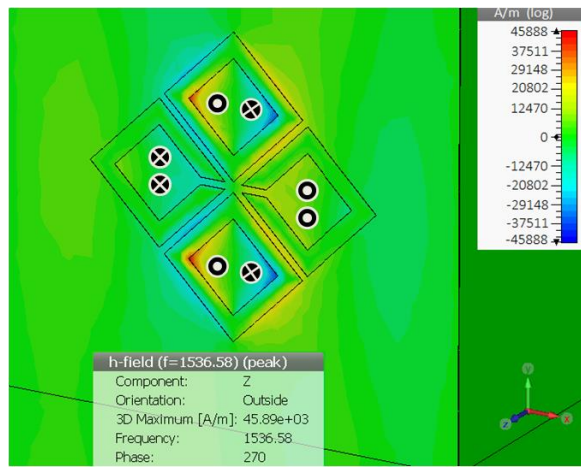


b) At phase 180°.

Fig. 13. Electric field intensity distribution for a full excitation cycle, for the main mode.



a) At phase 90°.



b) At phase 270°.

Fig. 14. Magnetic field intensity distribution for a full excitation cycle, for the main mode.

#### 4.2 Matched impedance feeder port

The antenna's overall impedance is nearly two times higher than the capacitive SRR-RA configuration, since inductive reactance is proportional to the operation frequency. With a  $400\ \Omega$  matched feeder port (port 3) connected, the amount of incident radiation coupled to this port (S31) verifies the antenna's latter S21 response. The impact of the inductively coupled SRRs on the antenna response is clear from the enhanced detection amplitude, that is here almost doubled.

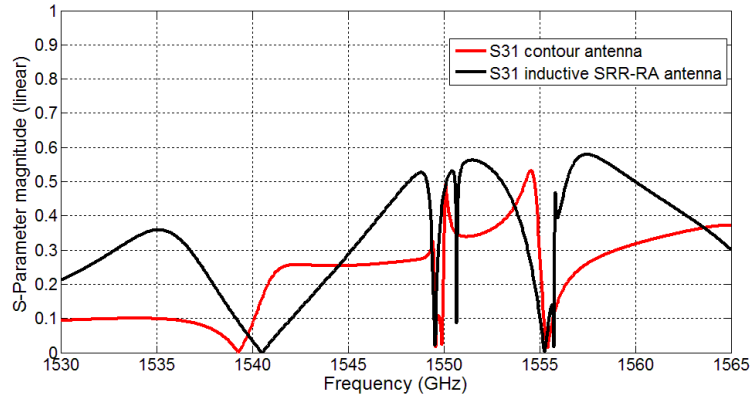


Fig. 15. Overlay of the S31 responses of the contour and inductive SRR-RA antennas.

## 5. Conclusion

We have computationally demonstrated the efficacy of SRR-RA antennas for efficient detection of THz-frequency beams. Enhanced detection arises from the coupling between the individual resonances of the SRRs and the contour. The coupling strength can be tuned by varying the coupling parameters, whose tuning allows for variable antenna impedance and for enhanced matching with the detector circuit. Furthermore, our novel design supports real-time modulation of the antenna impedance and resonant modes with the aid of gated graphene in the SRRs cut region.

The focus of our work is to introduce the feasibility of SRR assistance in the detection of THz radiation. Further detection enhancements are foreseen by exploiting alternative geometries and coupling parameters, and/or by using more refined SRRs.

## Acknowledgment

The authors acknowledge the EU-COST action MP 1204 TERAMIR.